Rotorcraft comprehensive code assessment for blade-vortex interaction conditions

Massimo Gennaretti, Giovanni Bernardini, Jacopo Serafini, Gianluca Romani[1]

Roma Tre University, Department of Engineering, 00146, Rome, Italy

Abstract

The scope of this paper is the presentation of the computational methodologies applied in the comprehensive code for rotorcraft developed in the last years at Roma Tre University, along with the assessment of its prediction capabilities focused on flight conditions characterized by strong blade-vortex interactions. Boundary element method approaches are applied for both potential aerodynamics and aeroacoustics solutions, whereas a harmonic-balance/modal approach is used to integrate the rotor aeroelastic equations. The validation campaign of the comprehensive code has been carried out against the well-known HART II database, which is the outcome of a joint multi-national effort aimed at performing wind tunnel measurements of loads, blade deflection, wake shape and noise concerning a four-bladed model rotor in low-speed descent flight. Comparisons with numerical simulations available in the literature for the same test cases are also presented. It is shown that, with limited computational cost, the results provided by the Roma Tre aero-acousto-elastic solver are in good agreement with the experimental data, with a level of accuracy that is in line with the state-of-the-art predictions. The influence of the vortex core modeling on aerodynamic predictions and the influence of the inclusion of the fuselage shielding effect on aeroacoustic predictions are discussed.

Keywords: helicopter rotors, aeroelasticity, aerodynamics, aeroacoustics

---

[1]Currently PhD student at Delft University of Technology, AWEP Department, 2629HS Delft, The Netherlands.

1. Introduction

Comprehensive codes represent a fundamental support for the modern rotorcraft design, often aiming at the development of new concept configurations. Indeed, typically composed of the combination of engineering models for the description of rotor structural dynamics (for instance, through beam-like blade representations) and unsteady aerodynamics (for instance, through coupling two-dimensional section models with wake influence from free-wake approaches), these offer lower-cost, reduced-order computational simulations of rotorcraft with respect to higher-accuracy CFD/CSD solvers, thus allowing a fast determination of the trend of the influence of parameter variations on design and often physical insight, as well [1, 2].

The HART II test campaign [3, 4, 5] is the best-known experimental campaign on helicopter rotor aerodynamics, aeroelasticity and aeroacoustics, performed at the DNW low-speed wind tunnel by a joint multinational effort of DLR (Germany), AFDD and NASA Langley (USA), Onera (France) and DNW (Netherlands), which provides an extensive database perfectly suited for comprehensive code validation purposes. Such database covers trim, elastic motion, aerodynamic loads, radiated noise, wake shape and flow velocity measurements for a four-bladed model rotor in low-speed descent flight.

It represents a challenging validation test in that this flight condition is difficult to simulate due to the complex interaction between rotor blades and wakes (Blade-Vortex Interaction, BVI) that takes place. The BVI phenomenon consists of the passage of a rotor blade through the vortices released by the other blades of the rotor. The aerodynamic effects produced by BVI are impulsive changes in blade loads that are particularly relevant in the blade span regions where the interaction occurs with the high-strength trailing tip vortices [6]. In turn, these give rise to high vibratory loads and external acoustic annoyance and hence have a great impact on cabin acoustic comfort, fatigue-life of structures, and on environmental and public acceptance of helicopters. For this reason, the availability of reliable tools for the prediction of BVI aerodynamic-aeroelastic-

aeroacoustic effects is of paramount importance for new generation helicopter design (strongly aiming at reducing both maintenance costs and noise levels), and hence the development of solvers suited for this task has captured the interest of many rotorcraft researchers.

In the years following the test campaign, several research centers and universities, including those involved in HART II, had been using the outcomes of the project for the validation of numerical codes dedicated to helicopter rotor analysis. The available literature includes a large number of works concerning assessments based on the correlation with HART II data of both comprehensive rotor codes (see, for instance Refs. [1, 2]) and CFD/CSD simulation approaches (see, for instance Refs. [7, 8]). In particular, Refs. [1, 2] provide also an overview of the methodologies used for the comprehensive codes developed by some international research centers and universities like, among the others, the U.S. Army Aeroflightdynamics Directorate (AFDD) and NASA team, Onera, DLR and the University of Maryland.

For instance, for the correlations presented in Refs. [1, 2], the AFDD and NASA team have used the CAMRAD II code [9], with the structural dynamics described through nonlinear finite beam elements, and the aerodynamic loads derived by combining the modified Onera ELDIN theory for unsteady aerodynamics [9] with C81 standard lookup table. A free-wake model with multiple trailers is applied.

A five-step computational method has been applied by Onera, composed of rotor trim, wake prediction, wake roll-up model, blade pressure computation, and finally noise radiation. The HOST comprehensive code [10] provided the aeroelastic blade response, with the structural model based on rigid beam elements with lumped elastic properties, and the aerodynamic loads derived from a lifting line theory which combines 2-D airfoil tables with the Theodorsen theory for unsteady aerodynamics. Firstly, a prescribed-helical-wake code is used to find trim condition and blade deformations, and then a full span free wake model is applied to evaluate blade pressure.

The researchers of the German Aerospace Centre (DLR) have used the com-

3

prehensive code S4, whose structural model consists of a finite element method based on the Houbolt and Brooks linear formulation for (flapwise and chordwise) bending and torsion of nonuniform rotor blades [11]. A semi-empirical analytic formulation for the airfoil coefficients, based on the Leiss method [12] for unsteady motion with enhancements suited for BVI problems, is used for modeling aerodynamics. Fuselage effects are introduced by an analytical formulation based on potential flow theory. The Mangler and Squire wake model is used to evaluate performance and vibrations, while an extension of the Beddoes prescribed wake [13] is used for noise evaluation.

The UMARC comprehensive code [14] has been used by the University of Maryland. The aeroelastic solver consists of a finite element method based on a non-linear, second-order, isotropic, Euler-Bernoulli beam model of the blade, loosely coupled with a lifting-line aerodynamic formulation and a free-wake solver.

All these teams have evaluated radiated noise through integration of the Ffwocs Williams and Hawkings equation [15] provided by Farassat's formulation 1A [16].

This paper presents an outline of the computational methodologies implemented in the comprehensive code for aero-acousto-elastic analysis of helicopter rotors developed at Roma Tre University in the last twenty years, as well as the assessment of the quality of its predictions through comparison with HART II data. The Roma Tre University comprehensive code is based on a harmonic-balance/modal approach [17] for the integration of the rotor aeroelastic equations obtained by coupling a beam-like model for the structural dynamics of slender, nonuniform, twisted blades, undergoing moderate displacement (inspired to that introduced in Ref. [18]) with the aerodynamic loads given by a boundary element method (BEM) solver for the solution of potential flows with free-wake modelling [19, 20]. The Farassat 1A integral formulation is applied for noise radiation.

In the next sections, first, the aeroelastic formulation (aerodynamics included) and the aeroacoustic formulation implemented in the computational

4

tool are outlined, and then the corresponding aerodynamic outcomes, aeroe-lastic response and radiated noise are correlated with HART II measurements.

These concern the tested four-bladed model rotor in low-speed, descent flight, for three different operating conditions: the baseline, in which only collective and cyclic trim controls are applied, and minimum-noise/minimum-vibration conditions obtained through application of suited $3/rev$ higher-harmonic controls (HHC).

2. The aero-acousto-elastic comprehensive code

The Roma Tre University comprehensive code includes the detailed aeroe-lastic response analysis of the blade within the trim procedure: the three-dimensional, potential-flow, rotor aerodynamics solver is fully coupled with a bending-torsion beam model of blade structural dynamics.

Hence, for a prescribed flight condition, the aeroelastic trim module provides pitch control settings and vehicle attitude, blade elastic response, mean and vibratory hub loads, as well as the pressure distributions required to define the noise sources in the aeroacoustic module (see the functional scheme of the code in Figure 1).

The main solution modules combined in the comprehensive code are briefly outlined in the following.

2.1. Blade structural dynamics

Blade structural dynamics is described through a beam-like model. It derives from a nonlinear, bending-torsion formulation valid for slender, homogeneous, isotropic, nonuniform, twisted blades, undergoing moderate displacements [18]. The radial displacement is eliminated from the set of equations by solving it in terms of local tension, and thus the resulting structural operator consists of a set of coupled nonlinear partial differential equations governing the bending of the elastic axis and the blade torsion [21].

These equations are spatially integrated through the Galerkin approach, with the elastic axis deformation and cross-section torsion described as linear

5
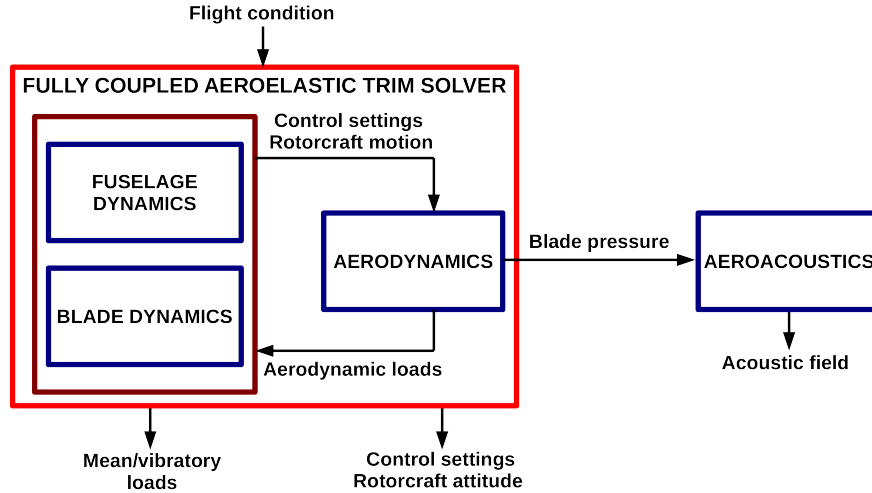
Figure 1: Sketch of the aero-acousto-elastic tool.

combinations of shape functions that satisfy homogeneous boundary conditions, thus yielding a set of nonlinear, ordinary differential equations of the type

$$M\ddot{q} + C\dot{q} + Kq = f_{str}^{nl}(q) + f^{aer}(q) \tag{1}$$

where q denotes the vector of the Lagrangean coordinates (time-variant coefficients of the linear combination of shape functions), M, C, and K are time-periodic mass, damping, and stiffness matrices representing the contribution of the linear structural terms. Nonlinear structural contributions are collected in the forcing vector f_{nl}^{str}, whereas the vector f^{aer} collects the generalized aerodynamic forces (namely, the projection of the distributed aerodynamic loads onto the shape functions).

2.2. Rotor unsteady aerodynamics

The aerodynamic loads are determined by a solver developed at Roma Tre University based on a BEM approach for the solution of unsteady potential flows around lifting bodies, that is capable of dealing with bodies in arbitrary motion, in the presence of strong blade-vortex interactions (BVI). It has been extensively

6

validated and successfully applied to aeroacoustic analyses of helicopter rotors (see, for instance, [22, 23, 24, 25]).

As presented in Ref. [19], for incompressible, potential flows such that $\boldsymbol{v} = \nabla\varphi$, the applied aerodynamic formulation considers the potential field, φ, to be given by the superposition of an incident field, φ_I, and a scattered field, φ_S (namely, $\varphi = \varphi_I + \varphi_S$). The scattered potential is determined by distributions of sources and doublets over the surface of the blades, S_B, and by doublets distributed over the wake portion that is very close to the trailing edge from which emanated (near wake, S_W^N). The incident potential field is associated to doublets distributed over the complementary far wake region, S_W^F. The wake surface partition is such that the far wake is the only wake portion that may come in contact with blades and generate BVI effects. The incident potential is discontinuous across S_W^F, whereas the scattered potential is discontinuous across S_W^N and is represented by [19]

$$\varphi_S(\boldsymbol{x}, t) = \int_{S_B} \left[G\left(v_n - u_n\right) - \varphi_S \frac{\partial G}{\partial n} \right] \mathrm{d}S(\boldsymbol{y}) - \int_{S_W^N} \Delta\varphi_S \frac{\partial G}{\partial n} \, \mathrm{d}S(\boldsymbol{y}) \qquad (2)$$

where $G = -1/4\pi\,r$ is the unit-source solution of the three-dimensional Laplace equation, with $r = \|\boldsymbol{y} - \boldsymbol{x}\|$, while $\Delta\varphi_S$ is the potential jump across the wake surface, known from past history of potential discontinuity at the blade trailing edge through the Kutta-Joukowski condition [22]. In addition, $v_n = \boldsymbol{v}_B \cdot \boldsymbol{n}$, with $\boldsymbol{v}_B$ and $\boldsymbol{n}$ representing blade velocity and outward unit normal, respectively, whereas $u_n = \boldsymbol{u}_I \cdot \boldsymbol{n}$, with $\boldsymbol{u}_I$ denoting the velocity induced by the far wake.

Considering the far wake discretized into panels, assuming the potential jump to be constant over each panel, and recalling the equivalence between surface distribution of doublets and vortices, the incident velocity field is given by the Biot-Savart law applied to the equivalent vortices having the shape of the contours of the panels. In order to assure a finite, regular distribution of the induced velocity, and thus a stable and regular solution even in BVI conditions, a Rankine finite-thickness vortex model is applied [19]. Wake-induced velocity field is applied to evaluate both the term u_n in Eq. (2), and the wake distortion for the free-wake analysis. Note that, for an accurate prediction of BVI phe-

7

nomena, the accurate evaluation of the wake shape is essential in that a crucial role is played by the relative position between body and wake vortices.

In this formulation, the incident potential affects the scattered potential through the induced-velocity, while the scattered potential affects the incident potential by its trailing-edge discontinuity that is convected along the wake and yields the intensity of the vortices of the far wake [19].

Once the potential field is known, the Bernoulli theorem yields the blade pressure distributions to be given to the aeroacoustic solver and provides the generalized forces, $\boldsymbol{f}^{aer}$, by projection onto the shape functions considered in the Galerkin approach (with introduction of a suited Prandtl-Glauert compressibility correction factor).

2.3. Aeroelastic coupling and trim

The rotor aeroelastic response for a steady flight is evaluated by integrating the nonlinear differential system in Eq. (1) through an iterative harmonic balance approach, with the generalized forces given by the BEM aerodynamic solver. Given a periodic blade bending-torsion deformation, the corresponding periodic aerodynamic loads are determined by a time marching integration scheme and these, in turn, yield a new periodic blade deformation from Eq. (1). This solution process is iterated until convergence, following the solution scheme of the Newton-Raphson method applied to the harmonic components of the blade deformation [17].

For trim purposes, the airframe equilibrium equations are coupled with the rotor aeroelastic equations, and hence suitably included in the iterative process: hub loads from the aeroelastic solution force the airframe equations which, in turn, provide blade pitch controls and rotorcraft attitude.

Blade pitch control setting, vehicle attitude, blade elastic response, mean and vibratory hub loads, blade airloads are the outputs of the aeroelastic trim solver.

8

2.4. Aeroacoustic solver

Given the blade pressure distribution, the rotor noise radiation is evaluated through the widely-used boundary integral formulation developed by Farassat [16] for the solution of the Ffowcs Williams and Hawkings equation [15], which governs the propagation of acoustic disturbances (acoustic pressure, p') aerodynamically generated by moving bodies.

When the velocity of the rotor blades is such that transonic effects are negligible, it gives the aeroacoustic field as a superposition of two terms: the thickness noise, p'_T, depending on blade geometry and kinematics,

$$4\pi p'_T(\boldsymbol{x}, t) = \int\limits_{S_B} \left[\frac{\rho_0 \dot{v}_n}{r|1 - M_r|^2} \right]_\tau \mathrm{d}S(\boldsymbol{y}) + \int\limits_{S_B} \left[\frac{\rho_0 v_n \left(r\dot{\boldsymbol{M}} \cdot \hat{r} + c_0 M_r - c_0 M^2 \right)}{r^2 |1 - M_r|^3} \right]_\tau \mathrm{d}S(\boldsymbol{y})$$

and the loading noise, p'_L, related to the distribution of pressure, p, over the blade surfaces,

$$4\pi p'_L(\boldsymbol{x}, t) = \frac{1}{c_0} \int\limits_{S_B} \left[\frac{\dot{\tilde{p}} \boldsymbol{n} \cdot \hat{\boldsymbol{r}} + \tilde{p} \dot{\boldsymbol{n}} \cdot \hat{\boldsymbol{r}}}{r|1 - M_r|^2} \right]_\tau \mathrm{d}S(\boldsymbol{y}) + \int\limits_{S_B} \left[\frac{\tilde{p} \boldsymbol{n} \cdot \hat{\boldsymbol{r}} - \tilde{p} \boldsymbol{M} \cdot \boldsymbol{n}}{r^2 |1 - M_r|^2} + \right]_\tau \mathrm{d}S(\boldsymbol{y})$$

$$+ \frac{1}{c_0} \int\limits_{S_B} \left[\frac{\tilde{p} \boldsymbol{n} \cdot \hat{\boldsymbol{r}}}{r^2 |1 - M_r|^3} r\dot{\boldsymbol{M}} \cdot \hat{\boldsymbol{r}} \right]_\tau \mathrm{d}S(\boldsymbol{y}) + \int\limits_{S_B} \left[\frac{\tilde{p} \boldsymbol{n} \cdot \hat{\boldsymbol{r}}}{r^2 |1 - M_r|^3} (M_r - M^2) \right]_\tau \mathrm{d}S(\boldsymbol{y})$$

In the above equations, $\boldsymbol{r}$ denotes the distance between observer position, $\boldsymbol{x}$, and source position, $\boldsymbol{y}$, whereas $\hat{\boldsymbol{r}} = \boldsymbol{r}/r$ is the unit vector along the source-observer direction, with $r = |\boldsymbol{r}|$. In addition, c_0, ρ_0 and p_0 denote, respectively, speed of sound, density and pressure in the undisturbed medium, the acoustic pressure is defined as $p' = c_0(\rho - \rho_0)$, $\tilde{p} = (p - p_0)$, $\boldsymbol{M} = \boldsymbol{v}_B / c_0$ with $\boldsymbol{v}_B$ denoting the body velocity, $M = \|\boldsymbol{M}\|$, $M_r = \boldsymbol{M} \cdot \hat{\boldsymbol{r}}$, and $v_n = \boldsymbol{v}_B \cdot \boldsymbol{n}$, where $\boldsymbol{n}$ is the outward blade surface unit normal vector. Furthermore, $\dot{\boldsymbol{n}}$ and $\dot{\boldsymbol{M}}$ denote time derivatives of $\boldsymbol{n}$ and $\boldsymbol{M}$ as observed in a frame of reference fixed with the undisturbed medium.

The integral contributions are evaluated by a zero-th order boundary element method, with the blade surface divided into quadrilateral panels, and the integrand functions multiplying kernels assumed to be uniformly distributed within each panel. Notation $[...]_\tau$ indicates that these quantities are evaluated

9

at the retarded time, $\tau = t - \theta$, where θ is the time taken by the signal started from $\boldsymbol{y} \in S_B$ to reach $\boldsymbol{x}$ at time t [16].

In problems dealing with weakly loaded rotors, thickness and loading noise are comparable. However, when strongly loaded rotors are examined (as in the case of BVI occurrence), the thickness noise tends to be negligible and the
acoustic disturbance is dominated by the loading noise.

3. Numerical results

In this section, the capability of the outlined aero-acousto-elastic tool of predicting BVI phenomena is assessed by correlation with HART II experimental data. Some numerical predictions available in the literature are included for
comparison, as well.

The rotor examined is the scaled model of the Bo-105 main rotor tested in the HART II program in the Large Low-speed Facility of the DNW [3, 4, 5]. The validation is carried out in terms of flowfield perturbations, blade airloads, aeroelastic response and noise emission. The HART II baseline configuration
(BL) consists of a rotor with four rectangular, hingeless blades having radius $R = 2$ m, chord $c = 0.121$ m, linear twist $\theta_{tw} = -8$ deg/R, rotational speed $\Omega = 109.12$ rad/sec, precone $\beta_p = 2.5$ deg, subject to a slipstream with advance ratio $\mu = 0.15$ and angle of attack (shaft angle) equal to 5.3-deg (descent flight condition). In addition to the BL case, minimum-noise (MN) and minimum-
vibration (MV) configurations are examined, both obtained by application of a 3/rev HHC with blade root pitch control angle of 0.8 deg, but differing for the control phases (equal to 180 deg and 300 deg, respectively). More details on rotor data and structural properties are available, for instance, in Ref. [2].

The predictions presented in the following are obtained by introducing a
torsion spring equal to 4985 Nm/rad to simulate the effect of the stiffness of the control system, as determined from the experimental data reduction given in Ref. [26], whereas no structural damping is included in the blade model. In addition, the complete rotor-fuselage configuration is considered in the aerody-

namic and aeroacoustic analyses, and the airframe/rotor trim is replaced with a procedure that determines the collective and cyclic pitch settings as those yielding the measured thrust ($T = 3300$ N), and rolling and pitching moments (20 Nm and -20 Nm, respectively).

Note that the numerical simulations are accomplished without inclusion of the wind tunnel interference correction of the shaft angle indicated in Ref. [2] in that, for arbitrary flight conditions, the comprehensive code assumes that interference effects are taken into account by reproducing hub loads through suited blade control settings.

Table 1 reports blade and fuselage discretization meshes, as well as the wake lengths, used for the BEM aerodynamic simulations. For the sake of computational cost saving, different meshes are applied for the evaluation of the Jacobian required by the iterative Newton-Raphson method (see Section 2.3), and for the periodic solution at each iteration step (the corresponding geometries of the fuselage-rotor system are shown in Fig. 2).

(a) *Jacobian*   (b) *Periodic solution*
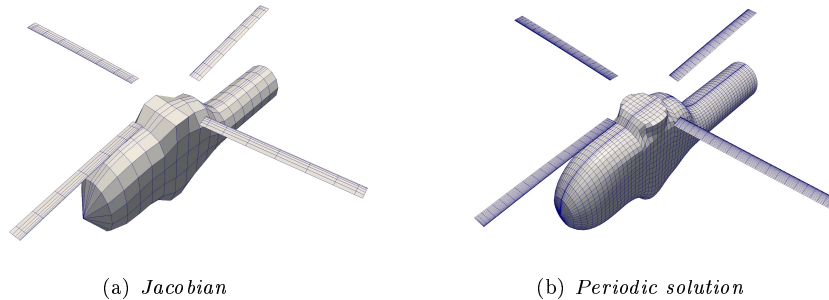
Figure 2: Fuselage-rotor discretized surfaces for harmonic-balance Jacobian and periodic solution evaluation.

Table 1:   Mesh parameters for blade, fuselage and wake discretization.

	blade panels	fuselage panels	wake age	wake panels
Jacobian	96	324	$720°$	480
Periodic solution	960	3660	$1440°$	1440

The next section presents predictions from the aerodynamic and aeroacous-

11

tic solvers based on blade deformation measured experimentally [27], in order to perform a specific assessment of their accuracy. Then, the results from the complete aero-acousto-elastic tool (thus, with blade deformation among the unknowns) are presented and compared both with the experimental HART II data and with the simulations performed by some of the research establishments and universities authoring Refs. [1, 2] (namely, the University of Maryland (UM) and the German Aerospace Centre (DLR)).

3.1. Aerodynamics and aeroacoustics correlations

Given the blade deformation obtained from the experimental data in Ref. [27], correlations of aerodynamic and aeroacoustic predictions with HART II measurements are presented in terms of normal force coefficient, tip-vortex trajectories and BVI noise radiation. Specifically, the blade elastic motion is described through the linear combination of three flap, three lead-lag and three torsion shape functions that coincide with the eigenfunctions of a bending-torsion uncoupled uniform cantilever beam. The Fourier coefficients of the first six harmonics of the Lagrangean coordinates are determined by a least square approximation of the time histories of the blade displacements provided at a given set of points along the blade span in Ref. [27].

3.1.1. Vortex core size

As described in Section 2.2, a crucial issue in the aerodynamic formulation implemented in the comprehensive code is the core size of the far wake vortices (namely, those that may impinge or pass very close to the rotor blades and hence produce BVI effects) [19]. Therefore, a preliminary analysis on vortex core size modeling is presented.

For r and ψ_v denoting, respectively, spanwise release position and age of the vortex (the latter expressed in terms of blade angular displacement), the core size, ε, is modeled through the following expression

$$\varepsilon(r, \psi) = \left[\varepsilon_r + \frac{r - r_c}{R - r_c} (\varepsilon_t - \varepsilon_r) \right] \sqrt{1 + \Delta\varepsilon\,\psi_v}$$

12

where r_c represents the root cut-off, $\varepsilon_r, \varepsilon_t$ denote, respectively, blade root and tip values of vortex core radius, whereas $\Delta\varepsilon$ is the rate of growth of the vortex core size. size. It yields a linear variation of the core size along the trailing edge, and a growth with age resembling that of the boundary layer over a flat plate.
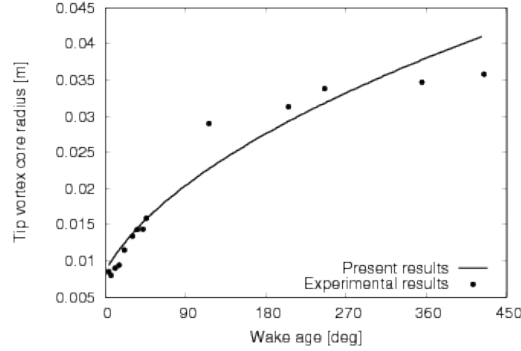

Figure 3: Variation of tip vortex core radius with wake age for $\varepsilon_t/c = 0.07$ and $\Delta\varepsilon = 3 \text{ rad}^{-1}$, BL case.

The values of ε_t and $\Delta\varepsilon$ have been determined as those providing the optimal correlation with the tip vortex core size growth evaluated in Ref. [28] starting from HART II measurements (see Fig. 3). For the definition of the inner vortex core size, ε_r, a sensitivity analysis of the accuracy of predicted loads on the ratio $\varepsilon_r/\varepsilon_t$ has been accomplished. The corresponding results are given in Table 2 in terms of the section loading coefficient, $c_n M^2 = L_s/[(\rho/2)\,c\,a_\infty^2]$ (with L_s and a_∞ denoting, respectively, section lift and speed of sound in the undisturbed medium). Specifically, it shows that the highest value of the Pearson correlation coefficient (PCC, measure of the linear correlation between numerical and experimental data) of $c_n M^2$ at $r/R = 0.87$ is obtained for $\varepsilon_r/\varepsilon_t = 5$ (further investigations have demonstrated that this value is optimal also for noise simulations).

Once the optimal values of $\varepsilon_r, \varepsilon_t$ and $\Delta\varepsilon$ have been determined by comparison with measurements, the influence of their variation on predicted section loading coefficient, $c_n M^2$, is examined in order to estimate the effect of vortex

13

Table 2: $c_n M^2$ PCC for different inner vortex core sizes.

$\varepsilon_r/\varepsilon_t$	$c_n M^2$ PCC
2	0.9212
5	0.9307
7	0.9152
8	0.9247
9	0.9184

core size uncertainty arising when experimental correlation data are unavailable. Figure 4(a) shows mean value, $\bar{\mu}$, and standard deviation, σ, of airloads at the blade section $r/R = 0.87$ obtained by considering variations equal to $\pm 50\%$ of the optimal values of ε_r and ε_t. Unexpectedly, the corresponding variation of $c_n M^2$ in the non-BVI regions has, at least, the same order of magnitude of that observed where BVI occurs. On the other hand, Fig. 4(b) depicts the influence of $\Delta \varepsilon$ variation ($\pm 50\%$ with respect to its optimal value). In this case, airloads are almost unaffected in non-BVI regions. This proves that the initial vortex core size affects airloads throughout the entire blade revolution and hence low-frequency loads, whereas its rate of growth is more influential on BVI phenomena and corresponding high-frequency effects.

(a) $\pm 50\%$ variations of optimal ε_r and ε_t (b) $\pm 50\%$ variations of optimal $\Delta \varepsilon$
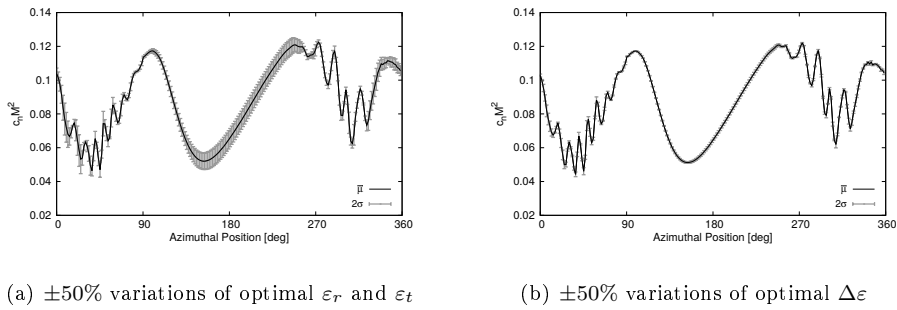
Figure 4: Mean value and standard deviation of $c_n M^2$ at $r/R = 0.87$, BL case.

3.1.2. Airloads

Given the optimal size of the core of the wake vortices, the correlation be-
tween experimental data and numerical predictions starts with the application
of the trim algorithm for the identification of the blade pitch control settings
providing measured thrust and hub moments. Table 3 presents the difference
between the control settings evaluated by the computational tool and the ex-
perimental data, for the three configurations examined. Because of the choice
of neglecting the wind tunnel interference correction of the shaft angle (con-
sisting of a reduction of about 0.8 deg [2]), the identified collective controls are
significantly underestimated with respect to the experimental values (of a quan-
tity that may be demonstrated to be correlated to the shaft angle correction),
whereas the discrepancies concerning the cyclic controls are smaller and in line
with those shown by the comprehensive codes considered in Ref. [2].

Table 3: Difference between numerical and experimental control settings.

	BL	MN	MV
$\Delta\theta_0$ [deg]	-0.71	-0.65	-0.75
$\Delta\theta_c$ [deg]	-0.31	-0.45	-0.32
$\Delta\theta_s$ [deg]	-0.12	-0.09	-0.04

Next, using the identified pitch control and the optimal vortex core size,
Figs. 5(a)–5(c) compare the time history of the section loading coefficients,
$c_n M^2$, predicted by the numerical tool with those measured in the wind tunnel
test. They concern, respectively, the BL, MN and MV configurations, with
mean values removed. In all cases the aerodynamic solver well predicts BVI in
terms of amplitude of induced load peaks and azimuthal position. In particular,
comparing Fig. 5(a) with Fig. 5(b) shows that the slightly delayed occurrence
of advancing side BVI appearing in the measured loads of the MN case is well
captured by simulations (note that it causes weaker BVI strength and noise due
to the resulting larger angle between blade and tip vortex). Similarly, the earlier
occurrence of the advancing side BVI in the MV case is also correctly predicted

(see Fig. 5(c)).

(a) BL case

(b) MN case

(c) MV case
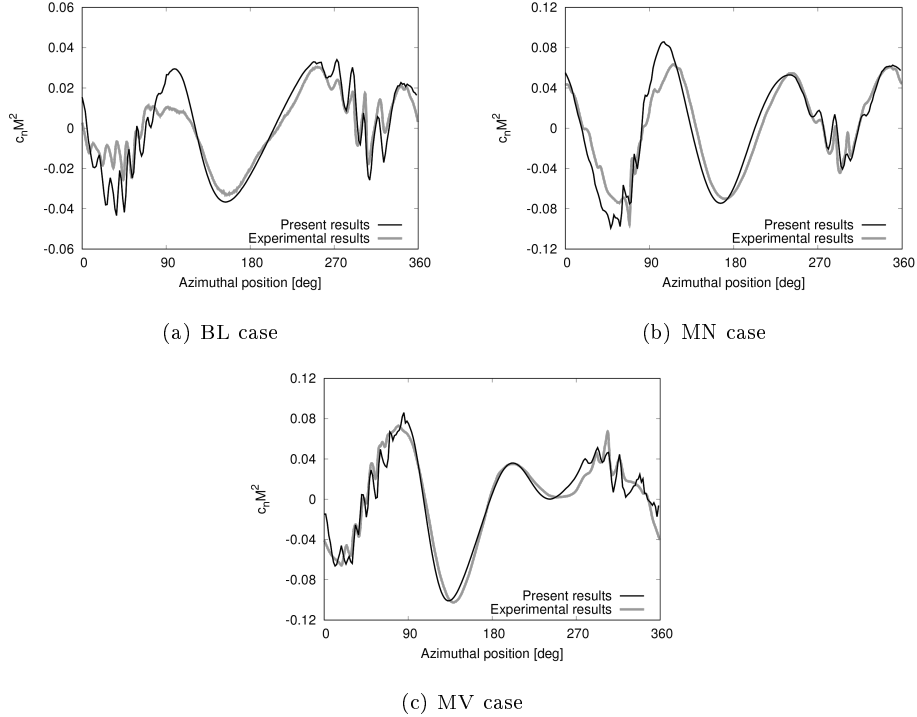
Figure 5: Time history of $c_n M^2$ at $r/R = 0.87$.

For a more detailed assessment of the capability of the prediction tool to
capture BVI effects, low-frequency and high-frequency contents of $c_n M^2$ are ex-
amined separately. The former is mostly affected by blade rigid and elastic mo-
tion (prescribed, in this analysis), and the quality of the numerical-experimental
correlation may be considered as a measure of the quality of blade motion and
overall loading prediction. Instead, the high-frequency signal is dominated by
the BVI events, and the accuracy of its prediction is strictly related to the capa-
bility of simulating wake shape and unsteady airloads. Concerning the baseline
case, Fig. 6(a) shows the comparison between the experimental and simulated
$c_n M^2$ low-frequency contents (including the first ten harmonics), whereas the
correlation of the high-frequency content (including harmonics higher than the
10/rev one) is depicted in Fig. 6(b). Both figures show good quality numeri-

16

cal results; in particular, Fig. 6(b) highlights the capability of the aerodynamic solver to predict intensity and position of BVI effects on airloads.

(a) low-frequency ($\leq 10/\text{rev}$)

(b) high-frequency ($> 10/\text{rev}$)
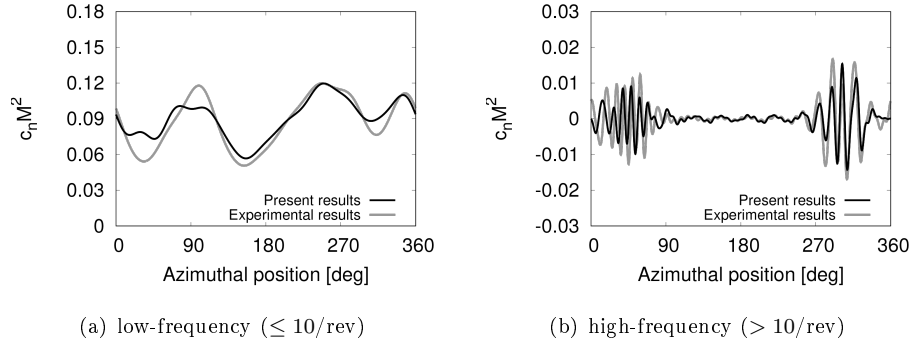
Figure 6: Time history of low- and high-frequency contents of $c_n M^2$ at $r/R = 0.87$, BL case.

3.1.3. Tip-vortex trajectory

Then, the data on the wake shape derived from the flow visualizations made within the project HART II are considered. Figure 7 shows the top view of the trajectories of the tip vortices released by the four blades for the BL case (those from the BEM simulation are identifies as the averaged position of the three outer far wake trailed vortices). The comparison between numerical and

(a) $\Psi = 20$ deg
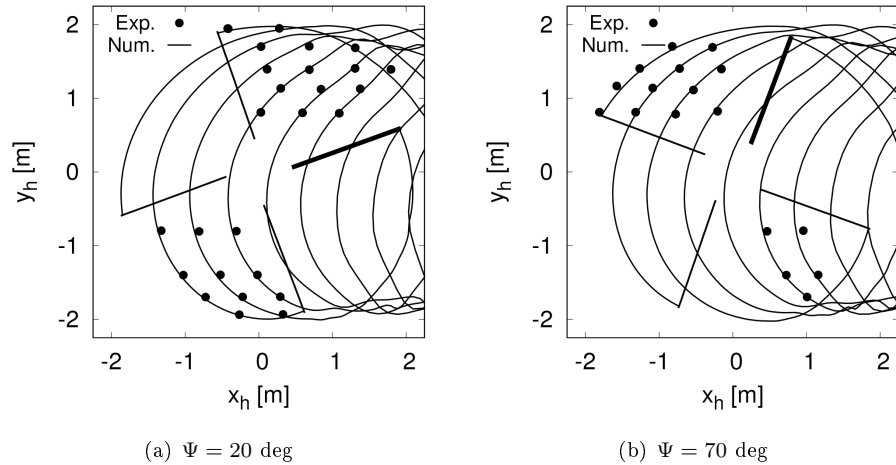
(b) $\Psi = 70$ deg

Figure 7: Top view of tip vortex trajectories, BL case.

17

experimental data is performed for two different azimuth rotor positions, $\Psi = 20$ deg and $\Psi = 70$ deg, and in both cases they are in excellent agreement both at the advancing and at the retreating side.

Next, in order to assess the capability of the numerical solver to predict the miss distance between blade and previously released vortices (the key factor of BVI), the tip vortices traces on two lateral planes, one at $y_h = 0.7R$ on the advancing side, and the other at $y_h = -0.7R$ on the retreating side, are considered (see Fig. 8). These planes are thought to be the most representative ones for BVI analysis, since they are crossed by the blades in the regions where BVIs occur.
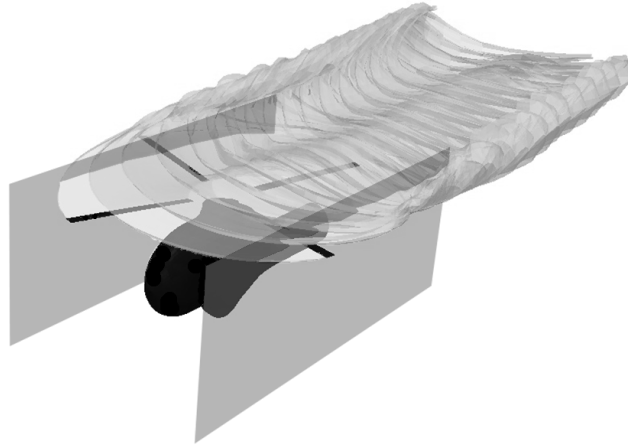
Figure 8: Longitudinal planes for identification of tip vortex trace.

Figures 9–11 show the comparisons of the traces evaluated numerically with those measured in the wind tunnel tests for the BL, MN and MV cases. Note that they are related to the blade azimuth position of $\psi = 20$ deg for $x_h > 0$, and $\psi = 70$ deg for $x_h < 0$ (x_h denotes the longitudinal coordinate, positive backwards). The aerodynamic solver reproduces with good accuracy the curvature and the vertical position of the wake traces and is able to capture the effects of the HHC on the wake shape. In particular, in the MN case it predicts the downward displacement of the wake as compared to the baseline case (see

Fig. 10 and Fig. 9). This displacement occurs together with a blade upward deformation, thus leading to an increase of the blade-vortex miss distance and hence to noise reduction. Opposite effects occur in the MV case (see Fig. 11).


(a) advancing side ($y_h = 0.7R$)   (b) retreating side ($y_h = -0.7R$)
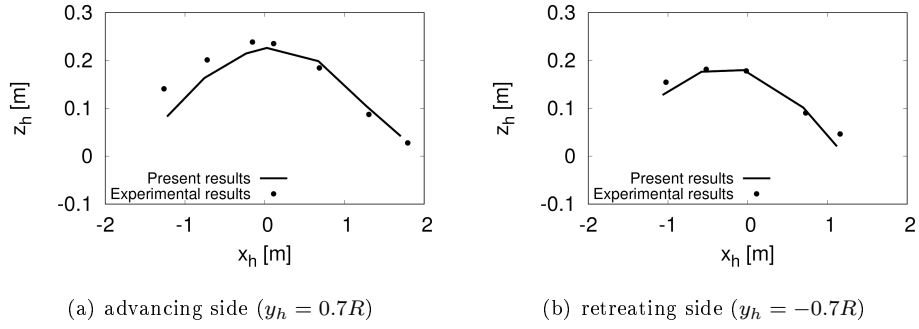
Figure 9: Tip vortex trace on longitudinal planes, BL case.

(a) advancing side ($y_h = 0.7R$)   (b) retreating side ($y_h = -0.7R$)
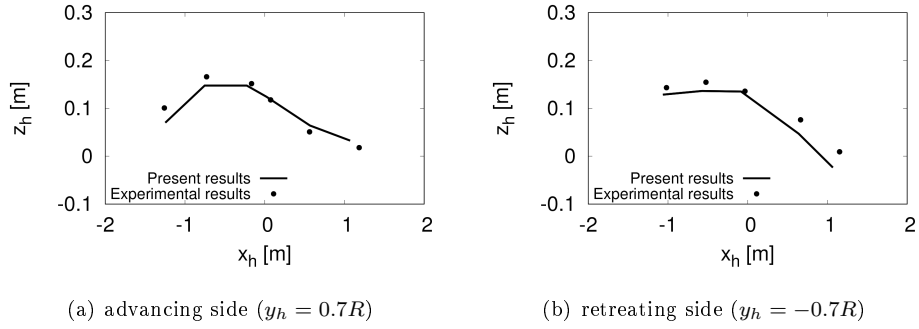
Figure 10: Tip vortex trace on longitudinal planes, MN case.

(a) advancing side ($y_h = 0.7R$)   (b) retreating side ($y_h = -0.7R$)
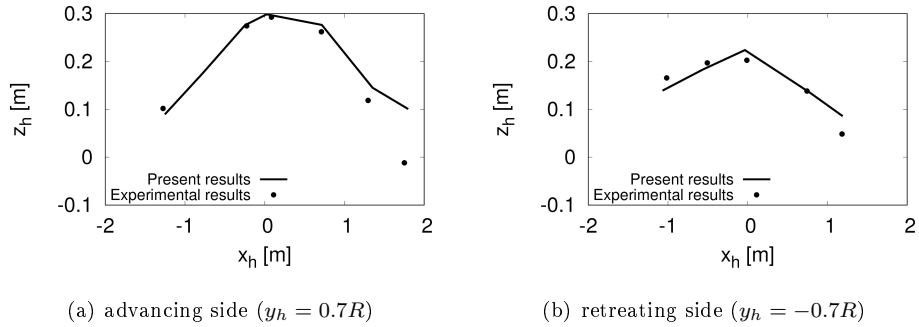
Figure 11: Tip vortex trace on longitudinal planes, MV case.

19

3.1.4. Radiated noise

The correlation between numerical predictions and experimental measurement of the aeroacoustic field is examined in terms of noise carpets computed/measured on a plane placed $1.1075R$ below the rotor hub, within a rectangular region of streamwise length $4R$ and lateral span $2.7R$, centered on the rotor hub vertical projection (noise was acquired by thirteen microphones equally spaced in lateral direction, at seventeen equally spaced streamwise positions). Specifically, the noise carpets are given in dB and concern the so-called BVISPL, which is the mid-frequency noise level including contributions from the 6th to the 40th blade passage frequency (bpf). The selected range of noise is that more affected by BVI events, and hence provides a direct estimation of the acoustic disturbance caused by BVI.

Figures 12–14 show the comparisons between noise contour maps predicted by the computational tool and those measured in the HART II project, respectively for the BL, MN and MV cases. The agreement is very good both in terms of noise levels and directivity, particularly for the BL and MV cases. These results demonstrate the capability of the aeroacoustic tool to capture the presence of two distinct regions of high-level noise (typical of low-speed descent flight), although the retreating side noise peak is slightly underestimated.

3.1.5. Fuselage effect

Finally, some of the aerodynamic and aeroacoustic predictions presented above are compared with those obtained for the isolated rotor, namely excluding the fuselage from the analysis. The fuselage presence affects the wake shape (although not remarkably in descent flights like those considered here) and acts as a scatterer for the pressure waves (particularly those in the higher portion of the $6^{th} - 40^{th}$ bpf BVI spectrum range, which have lengths comparable with the typical lengths of the obstacle).

For the BL case, Fig. 15(a) shows the predicted histories of $c_n M^2$ at $r/R = 0.87$, with and without inclusion of the fuselage beneath the rotor, whereas Fig. 15(b) depicts the influence of the fuselage on $c_n M^2$ over the whole rotor
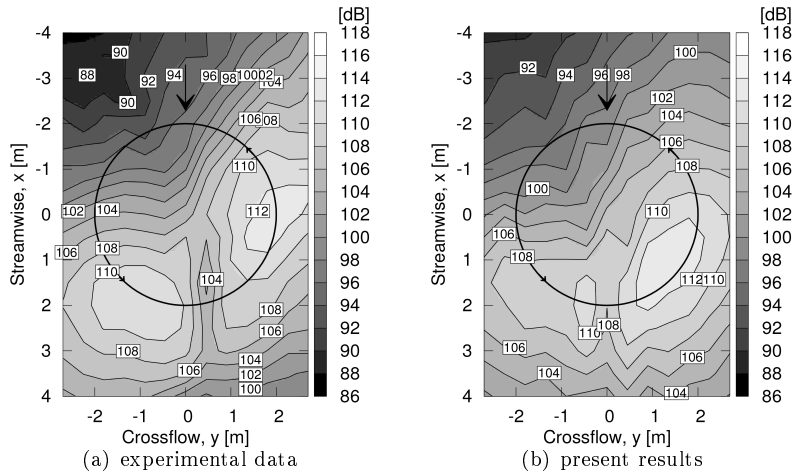
Figure 12: BVISLP noise contour levels, BL case.

Figure 13: BVISPL noise contour levels, MN case.

disk through a contour plot of the associated airload variations. Both low-spatial-frequency and high-spatial-frequency effects are observed in Fig. 15(b), the former appearing in fore and aft areas, and the latter appearing in the rear part of the advancing and retreating sides of the rotor disk, clearly related to the effects observed in Fig. 15(a) in the BVI affected regions.

The fuselage impact on noise is shown in Fig. 16, which depicts the contour

21
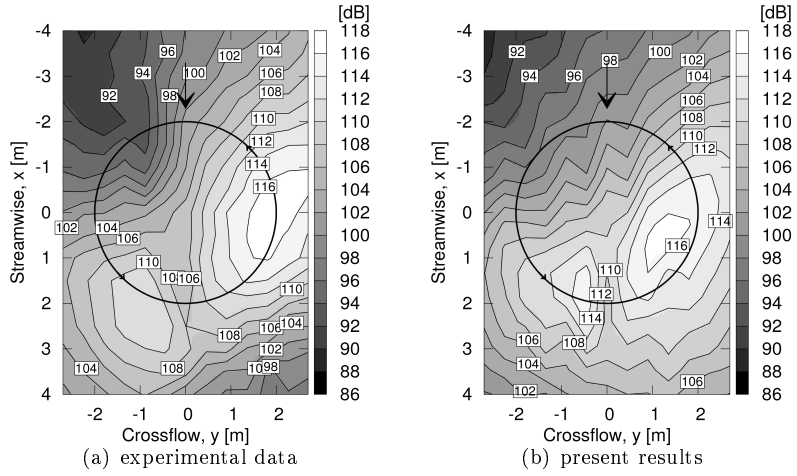
Figure 14: BVISPL noise contour levels, MV case.

(a) Time history at $r/R = 0.87$

(b) Rotor disk distribution of $\Delta c_n M^2$
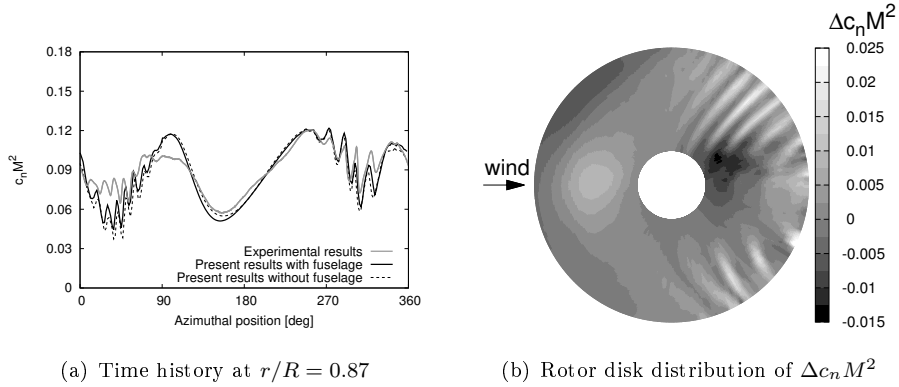
Figure 15: Effect of fuselage on $c_n M^2$, BL case.

plot of the differences of the noise predictions on the carpet of microphones obtained by considering isolated and non-isolated rotor. It demonstrates that the main scattering (shielding) effects arise in the fore and aft central areas of the noise carpets (just below the fuselage), with not negligible peaks.

3.2. Aero-acousto-elastic correlations

In this section, airloads, wake shape and noise predictions are provided by the complete comprehensive tool, and hence derive from the blade deformations

22
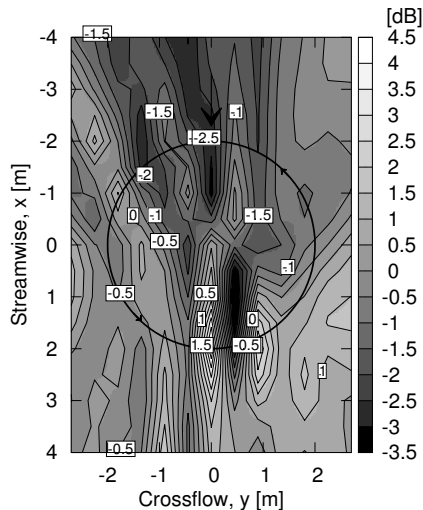
Figure 16: Effect of the inclusion of the fuselage on aeroacoustics.

evaluated by the aeroelastic solver.

3.2.1. Aeroelastic response

405   First, the periodic blade deformations evaluated by the comprehensive tool are correlated with experimental data in terms of blade tip flap, lead-lag and torsion deflections, and compared also with those obtained by the UM and DLR solvers and presented in Ref. [2].

Note that the motion of all four blades was measured in HART II, and sys-

410   tematic discrepancies appear between them. For this reason, in the correlations concerning the blade motion presented in the following, the experimental data related to all the four blades are shown. One reason for this non uniform behavior is the retro-fit of blade 1 (the reference blade) and blade 4, both equipped with several pressure sensors. Indeed, this alters their elasto-mechanical behav-

415   ior and hence structural response, with respect to the non-instrumented original blades [2].

For the BL, MN and MV flight configurations, Fig. 17 presents the numerical-experimental comparisons of the blade tip flap deflection time histories. The amplitude of the $1/rev$ harmonic of the present prediction appears smaller than

23

(a) BL case

(b) MN case

(c) MV case
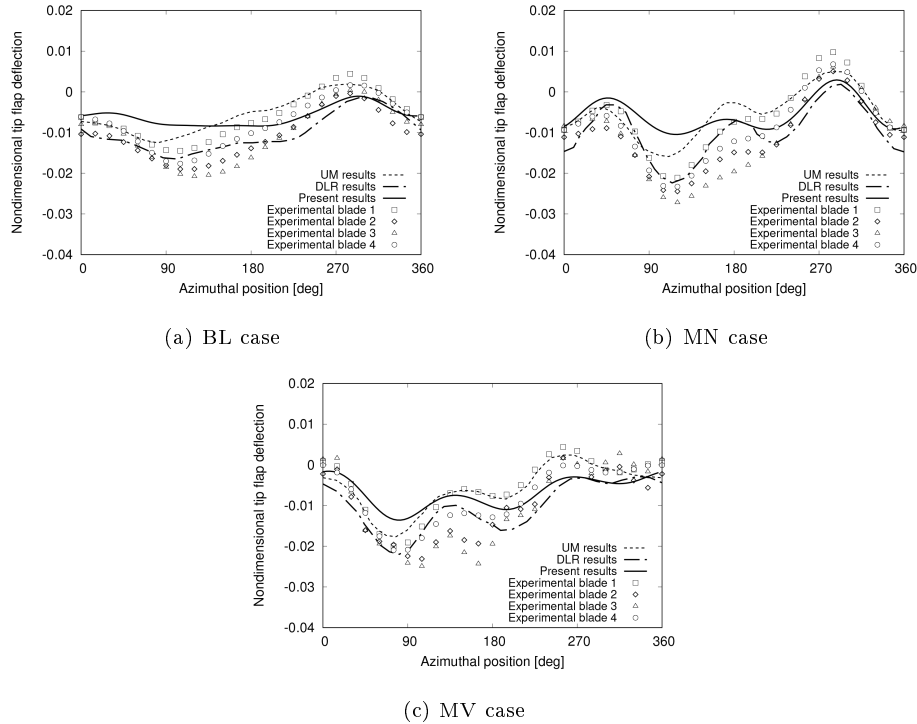
Figure 17: Time history of blade tip flap deflection.

that of the experimental data, with particular underestimation of the advancing side response. For the case with HHC actuation, the $3/rev$ harmonic content seems to be fairly well captured by the present aeroelastic tool, although smaller than that shown by the other numerical predictions shown (see Figs. 17(b) and 17(c)).

The blade tip lead-lag motion is examined in Fig. 18. In this case, the results are shown with mean value neglected, in that the experimental data are affected by a measurement systematic error that manifests as an offset of $0.0048R$ at the blade bolt independent of the azimuth position [27]. The comparisons shown in Figs. 18(a)–18(c) demonstrate that the lead-lag dynamic response predicted by the present tool is in very satisfactory agreement with measurements.

The blade torsion is shown in Fig. 19. Similarly to the experimental data, a 2/rev harmonic appears in the BL case, although some discrepancies are present

24

(a) BL case
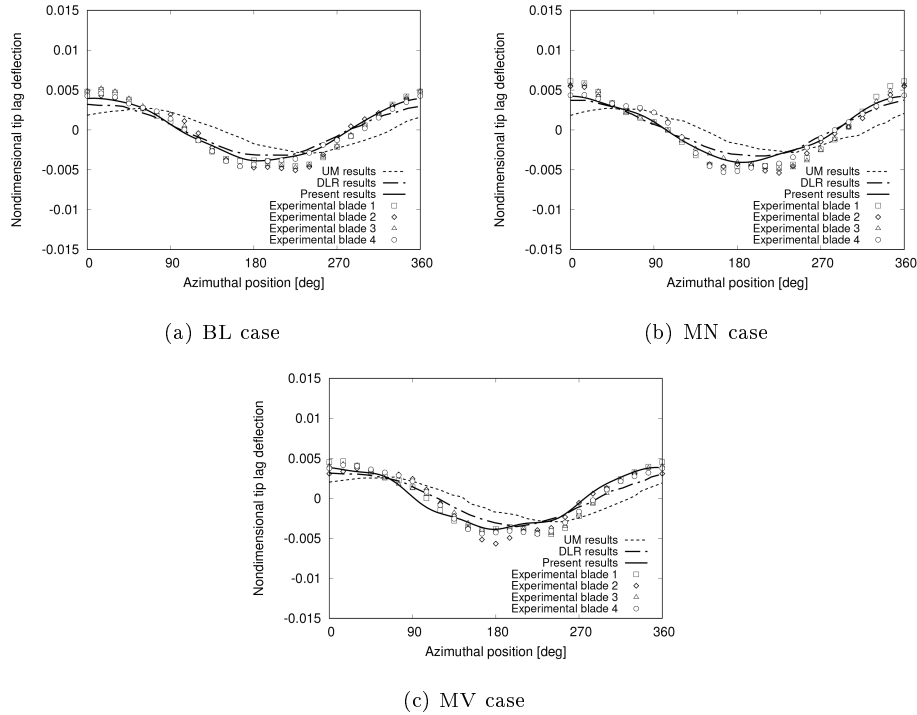
(b) MN case

(c) MV case

Figure 18: Time history of blade tip lead-lag deflection.

in the advancing region. Considering the HHC cases, the 3/rev harmonic content of the blade torsional response is fairly captured in the MN case, whereas in the MV case discrepancies between present numerical results and experimental data arise in the advancing side. It is worth noting that, taking into account also the numerical predictions from other computational tools, the elastic torsion is the blade motion showing the weakest numerical-experimental correlation (see also Ref. [2])

3.2.2. Tip vortex trajectory and airloads

For the rotor azimuth positions $\Psi = 20$ deg and $\Psi = 70$ deg, Figs. 20(a) and 20(b) show the comparison between the top view of the tip vortex trajectories evaluated in the present aeroelastic analysis and those observed in the experiments, for the BL case. The similarity is very satisfactory both in the

25

(a) BL case

(b) MN case

(c) MV case
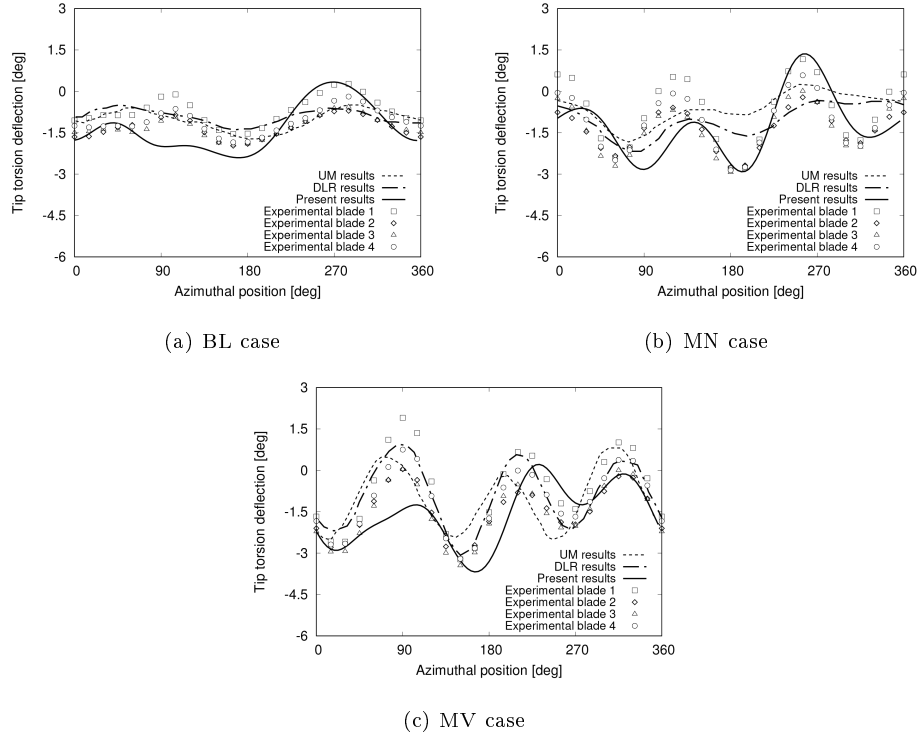
Figure 19: Time history of blade tip torsion deflection.

advancing and retreating sides, with a quality of results comparable to that obtained by the prescribed blade motion approach, thanks to the fact that the inaccuracies in the evaluation of blade deformations mainly affect the vertical position of wake vortices. Indeed, for the tip-vortex traces on the vertical planes illustrated in Fig. 8 the numerical-experimental correlation is worse, as shown in Fig. 21, where the predictions by UM and DLR are presented for comparison (see Ref. [2]). This occurs especially in the advancing side and downstream the rotor hub (namely, for $x_h > 0$), where the present aeroelastic simulations underestimate the blade flap motion (see Fig. 17(a)). Nevertheless, the aeroelastic prediction of the wake geometry remains quite satisfactory, also if compared with results from the literature, and this is confirmed for the MN and MV cases (not shown here for the sake of conciseness).

Next, Fig. 22 presents the $c_n M^2$ coefficient at $r = 0.87R$, for the three op-

26

(a) $\Psi = 20$ deg   (b) $\Psi = 70$ deg
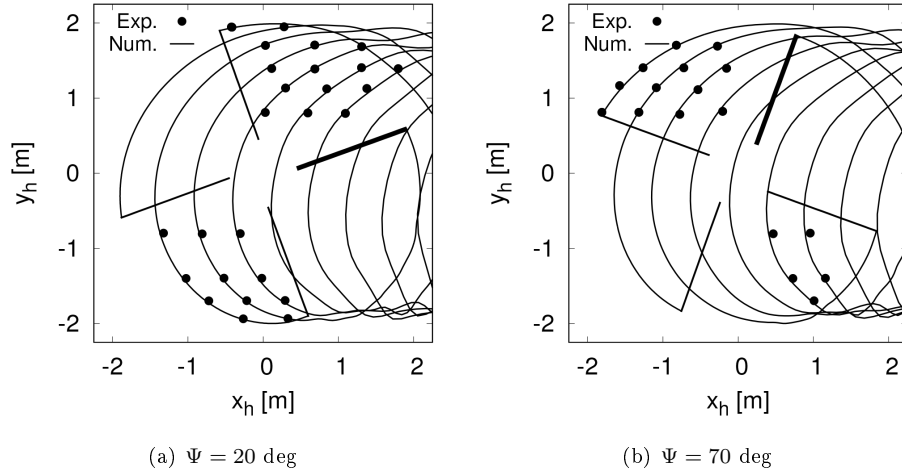
Figure 20: Top view of tip vortex trajectories, BL case.

(a) advancing side ($y_h = 0.7R$)   (b) retreating side ($y_h = -0.7R$)
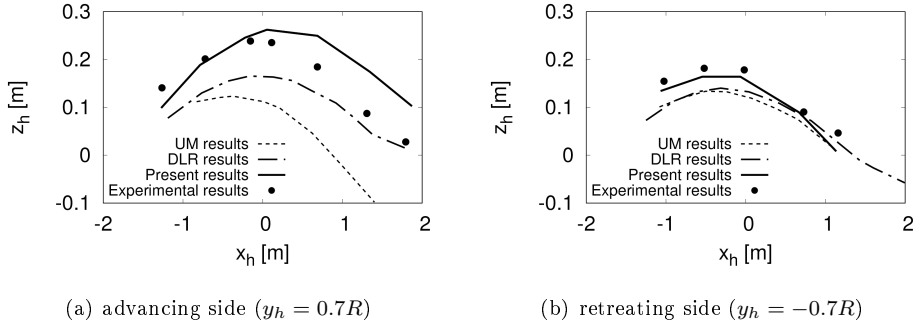
Figure 21: Tip vortex trace on longitudinal planes, BL case.

erating conditions with removed mean values. Akin to the aeroelastic response, the experimental data are correlated with the present tool predictions as well as with those from the UM and DLR comprehensive codes [2]. Despite of the inaccuracies arising in the evaluation of the blade deformations, the airloads from the present numerical simulations show a good level of correlation with the measured ones, with amplitude and azimuth of higher-frequency effects of BVI events quite well captured. This is confirmed in Figs. 23(a) and 23(b) which, for the BL case, represent the numerical-experimental correlation of the signals from, respectively, the low-frequency (≤ 10/rev) and high-frequency (> 10/rev)

27

harmonic components of the sectional airload. The larger discrepancies observed in Fig. 23(a) are strictly related to the inaccuracies of the blade motion predictions already shown in Figs. 17(a), 18(a) and 19(a). whereas Fig. 23(b) underlines the good capability of the aeroelastic solver to capture BVI effects.


(a) BL case

(b) MN case

(c) MV case
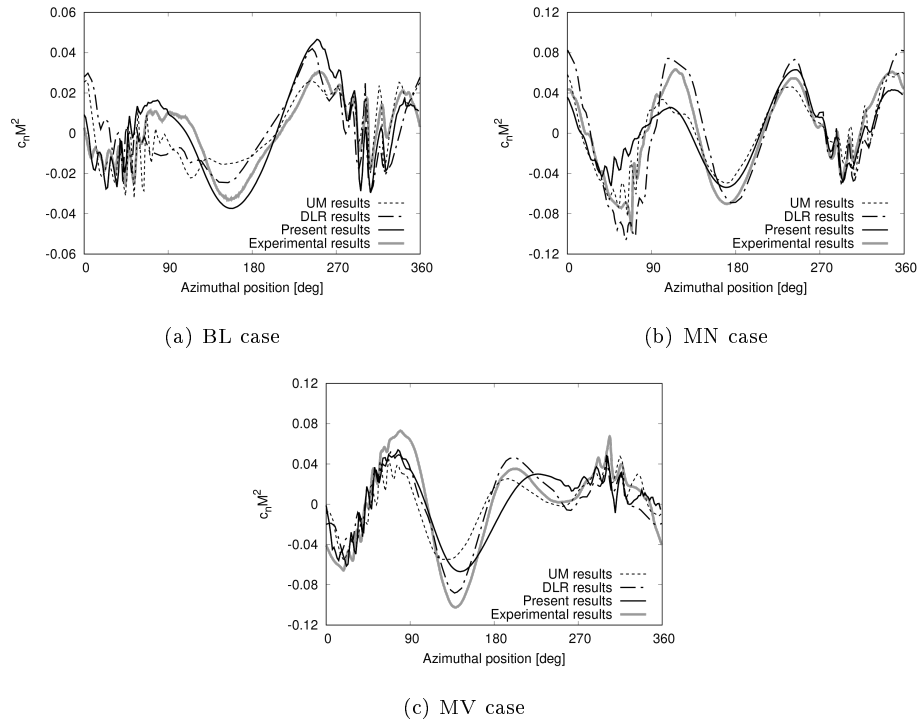
Figure 22: Time history of $c_n M^2$ at $r/R = 0.87$.

3.2.3. Radiated noise

Finally, Figs. 24–26, show BVISPL contour maps evaluated through the simulations provided by the comprehensive code with calculated blade deformations (and fuselage inclusion beneath the rotor). BVI noise directivity and peaks are still well predicted in the BL and MV cases, whereas a lower level of accuracy of the numerical simulations is observed for the MN condition for which, however, the associated reduced noise disturbance is fairly captured. It is worth noting that the quality of the present aeroacoustic predictions may be consid-

28

(a) low-frequency ($\leq 10/\text{rev}$) (b) high-frequency ($> 10/\text{rev}$)
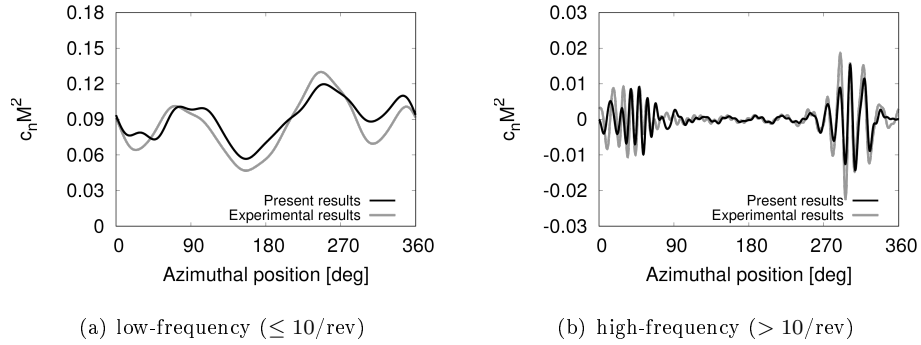
Figure 23: Time history of low- and high-frequency content of $c_n M^2$ at $r/R = 0.87$, BL case.

ered to be, at least, comparable to that of the results from the state-of-the-art comprehensive codes shown in Refs. [1, 2].


(a) experimental data (b) present results
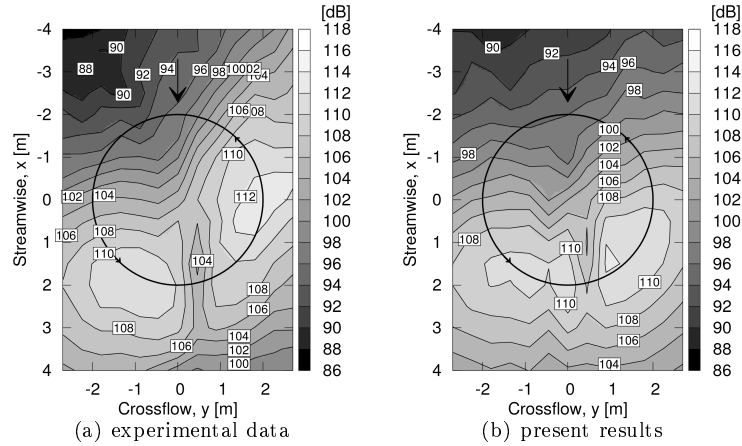
Figure 24: BVISPL noise contour levels, BL case.

480

4. Conclusions

The comprehensive aero-acousto-elastic code developed in the last years at Roma Tre University has been validated against the well known HART II database. The comparison has been performed over a wide set of results, including trim settings, aerodynamic loads, blade elastic motion, wake shape and radiated noise. Numerical results available in the literature have been considered

485

29
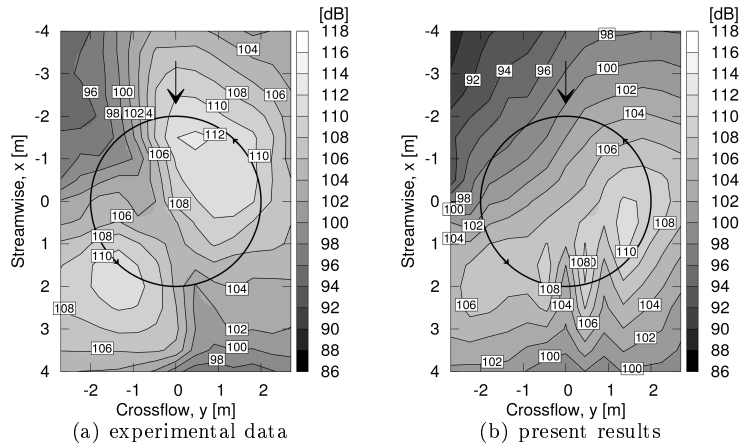
Figure 25: BVISPL noise contour levels, MN case.
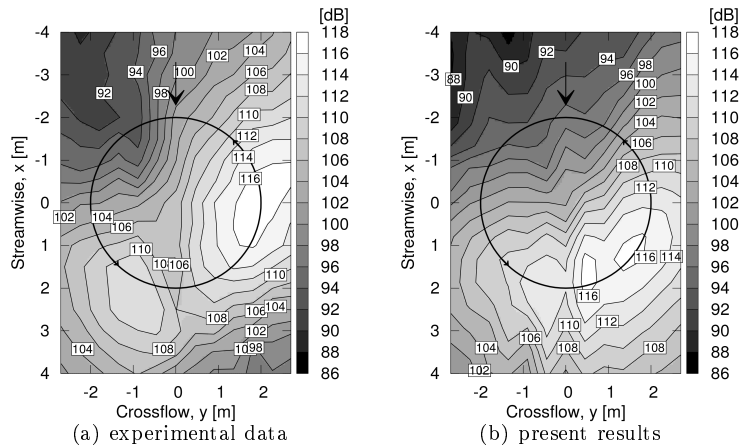
Figure 26: BVISPL noise contour levels, MV case.

for comparison. Preceded by a numerical investigation concerning the choice of the optimal wake vortex core size to be used in the simulations, aerodynamic predictions of wake shape and unsteady airloads, as well as aeroacoustic predictions of emitted noise show a very satisfactory correlation with experimental data. This result is achieved both when the simulation is based on the blade elastic motion measured in the wind tunnel tests, and when it is the result of the aeroelastic solver included in the comprehensive tool, although some inaccura-

cies are present in the evaluated flap and torsion deflections, particularly in the

495 advancing side region. In particular, the solver is capable of capturing intensity and location of aerodynamic loads induced by BVI phenomena, along with intensity and directivity of the corresponding radiated noise. It has been proven that including the presence of the fuselage beneath the rotor in performing the simulations provides a not negligible beneficial effect on the quality of the pre-

500 dicted blade airloads and emitted acoustic disturbance. In the overall, the level of accuracy of the results obtained by the proposed comprehensive code is in line with that of the simulations given by state-of-the-art comprehensive prediction tools. The computational cost is limited: the complete aero-acousto-elastic simulation is performed in a few hours by a common desktop PC.

505 **References**

[1] B. G. van der Wall, J. W. Lim, M. J. Smith, S. N. Jung, J. Bailly, J. D. Baeder, D. D. Boyd Jr, An assessment of comprehensive code prediction state-of-the-art using the HART II international workshop data, in: 68th Annual Forum of the American Helicopter Society, Ft. Worth, TX, 2012.

510 [2] B. G. van der Wall, J. W. Lim, M. J. Smith, S. N. Jung, J. Bailly, J. D. Baeder, D. D. Boyd Jr, The HART II international workshop: an assessment of the state-of-the-art in comprehensive code prediction, CEAS Aeronautical Journal 4 (3) (2013) 223–252.

[3] B. G. van der Wall, 2nd hhc aeroacoustic rotor test (hart ii)-part I: Test
515 documentation, Tech. Rep. IB 111-2003/31, DLR (2003).

[4] B. G. van der Wall, C. L. Burley, Y. Yu, H. Richard, K. Pengel, P. Beaumier, The HART II test–measurement of helicopter rotor wakes, Aerospace Science and Technology 8 (4) (2004) 273–284.

[5] B. G. van der Wall, C. L. Burley, 2nd hhc aeroacoustic rotor test (hart
520 ii)-part ii: Representative results, Tech. Rep. IB 111-2005, DLR (2005).

31

[6] C. Tung, Y. H. Yu, S. L. Low, Aerodynamic aspects of blade-vortex inter-
action (bvi), in: AIAA Paper 96-2010, 27th AIAA Fluid Dynamics Confer-
ence, New Orleans, LA, 1996.

[7] M. J. Smith, J. W. Lim, B. G. van der Wall, J. D. Baeder, R. T. Biedron,
D. D. Boyd Jr, B. Jayaraman, S. N. Jung, B.-Y. Min, An assessment
of CFD/CSD prediction state-of-the-art using the HART II international
workshop data, in: 68th Annual Forum of the American Helicopter Society,
Ft. Worth, TX, 2012.

[8] M. J. Smith, J. W. Lim, B. G. van der Wall, J. D. Baeder, R. T. Biedron,
D. D. Boyd Jr, B. Jayaraman, S. N. Jung, B.-Y. Min, The HART II in-
ternational workshop: an assessment of the state of the art in CFD/CSD
prediction, CEAS Aeronautical Journal 4 (4) (2013) 345–372.

[9] W. Johnson, Aerodynamic models for a comprehensive analysis, in: 54th
Annual Forum of the American Helicopter Society, Washington, DC, 1998.

[10] B. Benoit, A. M. Dequin, K. Kampa, W. GrÃijnhagen, P. M. Basset, B. Gi-
monet, Host, a general helicopter simulation tool for germany and france,
in: 56th Annual Forum of the American Helicopter Society, Virginia Beach,
VA, 2000.

[11] J. C. Houbolt, G. W. Brooks, Differential equations of motion for combined
flapwise bending, chordwise bending, and torsion of twisted nonuniform
rotor blades, Tech. Rep. TN 3905, NACA (1957).

[12] U. Leiss, A consistent mathematical model to simulate steady and un-
steady rotor-blade aerodynamics, in: 10th European Rotorcraft Forum,
The Hague, Netherlands, 1984.

[13] T. S. Beddoes, A wake model for high resolution airloads, in: AHS/ARO 1st
International Conference on Rotorcraft Basic Research, Research Triangle
Park, NC, 1985.

[14] I. Chopra, G. Bir, University of maryland advanced rotor code: Umarc, in: merican Helicopter Society Aeromechanics Specialists Conference, San Francisco, CA, 1994.

[15] J. F. Williams, D. L. Hawkings, Sound generation by turbulence and surfaces in arbitrary motion, Philosophical Transactions of the Royal Society of London A: Mathematical, Physical and Engineering Sciences 264 (1151) (1969) 321–342.

[16] F. Farassat, Derivation of formulations 1 and 1A of Farassat, Tech. Rep. TM-2007-214853, NASA (2007).

[17] G. Bernardini, J. Serafini, M. Molica Colella, M. Gennaretti, Analysis of a structural-aerodynamic fully-coupled formulation for aeroelastic response of rotorcraft, Aerospace Science and Technology 29 (1) (2013) 175–184.

[18] D. H. Hodges, E. H. Dowell, Nonlinear equation for the elastic bending and torsion of twisted nonuniform rotor blades, Tech. Rep. TN D-7818, NASA (1974).

[19] M. Gennaretti, G. Bernardini, Novel boundary integral formulation for blade-vortex interaction aerodynamics of helicopter rotors, AIAA Journal 45 (6) (2007) 1169–1176.

[20] M. Gennaretti, M. M. Colella, G. Bernardini, Prediction of tiltrotor vibratory loads with inclusion of wing-proprotor aerodynamic interaction, Journal of Aircraft 47 (1) (2010) 71–79.

[21] D. Hodges, R. Ormiston, Stability of elastic bending and torsion of uniform cantilever rotor blades in hover with variable structural coupling, NASA Technical Note TN D-8192, NASA (1976).

[22] M. Gennaretti, L. Luceri, L. Morino, A unified boundary integral methodology for aerodynamics and aeroacoustics of rotors, Journal of Sound and Vibration 200 (4) (1997) 467–489.

33

[23] G. Bernardini, J. Serafini, S. Ianniello, M. Gennaretti, Assessment of computational models for the effect of aeroelasticity on bvi noise prediction, International Journal of Aeroacoustics 6 (3) (2007) 199–222.

[24] M. Gennaretti, J. Serafini, G. Bernardini, A. Castorrini, G. De Matteis, G. Avanzini, Numerical characterization of helicopter noise hemispheres, Aerospace Science and Technology 52 (2016) 18–28.

[25] M. Gennaretti, G. Bernardini, J. Serafini, A. Anobile, S. Hartjes, Helicopter noise footprint prediction in unsteady maneuvers, International Journal of Aeroacoustics 16 (3) (2017) 165–180.

[26] B. G. van der Wall, Hart ii workshop database update, in: 8th HART II International Workshop, Hamburg, Germany, 2009.

[27] B. G. van der Wall, Mode identification and data synthesis of HART II blade deflection data, Tech. Rep. IB-111-2007/28, DLR (2007).

[28] M. E. Kelly, R. Brown, Predicting the wake structure of the HART II rotor using the vorticity transport model, in: 34th European Rotorcraft Forum, Liverpool, United Kingdom, 2008.